Torsional Shear Flow of Nematic and Cholesteric Liquid Crystals Part I: Nematic Phase

J. Wahl

Physikalisches Institut der Universität Münster

Z. Naturforsch. **34a**, 818–831 (1979); received April 6, 1979

The simple shear flow of a homeotropic nematic layer in an electric field normal to the layer is studied theoretically and experimentally. Several material constants of MBBA are determined as a function of temperature.

1. Introduction

The present work is an extension of a previously published work [1] on studying simple shear flow of liquid crystals. With new measuring equipment (Sect. 2), the torsional shear flow method (Sect. 2) is now used to study the influence of three experimental parameters on simple shear flow. These parameters are the temperature T, the electric voltage U and the eigentwist t_0, which can be induced by doping the nematic material with chiral molecules, thus obtaining a cholesteric liquid crystal. The shear flow of such cholesteric mesophases will be studied separately (Part II). In Part I we first outline some theoretical calculations for describing flow and electric field induced deformation patterns (Section 3). The hydrodynamic equations of Leslie and Ericksen [2, 3] are applied to the present problem and solved by computer techniques as well as by an approximation formalism in some limiting cases. The deformation patterns of the nematic layer are experimentally analyzed in detail and compared with the theoretical predictions (Section 4).

2. Experimental

As has been described previously [1, 4], the torsional shear cell consists of two circular glass plates (G) at an adjustable distance d (see Fig. 1). One of them can be rotated against the other with a constant angular frequency $\boldsymbol{\omega}$, thus obtaining a whole field of shear velocities ($\boldsymbol{v}$). The cell, containing the liquid crystal (LC), is positioned between two (linear) polarizers (P) and illuminated by normally incident monochromatic light (wavelength $\lambda = 546$ nm). The inner planes of the cell are coated with electrically conducting material (Baltracon *).

Based on this model of a shear cell, a very much improved version of the previously described measuring apparatus [1] has been built up. In the new apparatus, the two glass plates (radius $R \approx 3$ cm) of the shear cell are positioned at a distance of about 15 cm away from the adjustment and driving elements [1] on the top of two glass tubes which are fitted into one another. (The inner, rotating tube carries the lower plate). By a cylindrical oven, surrounding this glass system, the temperature of the cell can be stabilized up to 0.1 K within a range from about 275 K to 360 K. The oven is supplied with water of constant temperature. By external pressure gradients, desiccated air is forced to circulate within the oven, thus giving a sufficiently good heat transfer between the oven and the shear cell. Moreover, the new location of the cell allows measurements with horizontal and vertical magnetic fields.

The distance between the two glass plates (layer thickness d) can be adjusted continuously by a differential thread mechanism. The absolute value

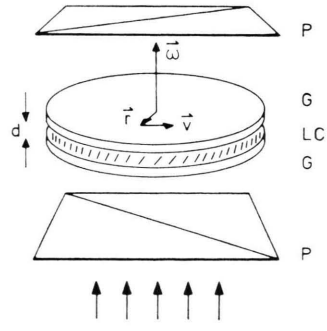

Fig. 1. Principle set up of the torsional shear cell.

* Product of Balzers AG, Liechtenstein.

Reprint requests to Dr. J. Wahl, Physikalisches Institut der Universität Münster, Schloßplatz 7, D-4400 Münster.

0340-4811 / 79 / 0700-0818 $ 01.00/0

of d is measured by a micrometer and, indirectly, by a capacitance bridge with a maximum error of 1 μm. A dc-servomotor drives the lower glass plate with a constant angular velocity ω ranging from $10^{-4}\,s^{-1}$ to $10^{-1}\,s^{-1}$. (The relative error of ω is about 0.1%.) The homeotropic boundary conditions are produced by coating the inner glass planes of the cell with an invisibly thin film of soja-lecithin (using a solution of lecithin in benzene). In order to avoid electrohydrodynamic flow [5], ac-voltages with a sufficiently high frequency (≈ 1 kHz) are used. For analyzing the textures of the liquid crystal layer, a self-made 6×6 cm reflex camera and a microscope are mounted onto the new measuring apparatus.

3. Theoretical Analysis

3.1. Numerical Computations

Excluding an area around the center of torsion, with a diameter of about ten times the layer thickness, the torsional shear flow locally will be approximated by (linear) simple shear flow. Typical director profiles of a sheared (initially homeotropic) layer are sketched in Fig. 2 for a) a nematic and b) a long pitch cholesteric liquid crystal (see Part II). In both cases the tilt angle ϑ of the director $\hat{n}$ increases with increasing shear velocity v up to the limiting flow alignment angle ϑ_0. The cholesteric helix completely unwinds for $v \to \infty$ (see Part II).

The equilibrium condition $\boldsymbol{\Gamma} = \hat{n} \times \boldsymbol{h} = 0$ ($\boldsymbol{\Gamma}$: total torque density) yields two independent second order differential equations for ϑ and φ (see Figure 2). Expressing the molecular field $\boldsymbol{h}$ [5] in terms of the hydrodynamic theory of Leslie and Ericksen [2, 3], one obtains from $\Gamma_z = 0$ the following equation for the stationary flow of the liquid crystal, using the reduced coordinate $\zeta = 2z/d$:

$$\frac{\mathrm{d}}{\mathrm{d}\zeta}\{\sin^2\vartheta[f_2(\vartheta)\,\varphi' - \tfrac{1}{2}(x_2+1)\,t_0\,d]\} + \gamma_K \frac{d}{8} u' \sin 2\vartheta \sin\varphi = 0\,. \tag{1}$$

The second equation is reasonably obtained from the condition $\Gamma_y n_x - \Gamma_x n_y = 0$:

$$f_1(\vartheta)\,\vartheta'' + \tfrac{1}{2}x_1 \sin 2\vartheta\,\vartheta'^2 + \tfrac{1}{2}\sin 2\vartheta\{\varphi'^2 + \varphi'[(x_2+1)\,t_0 d - 2f_2(\vartheta)\,\varphi']\} + \tfrac{1}{2}\sin 2\vartheta \frac{\pi^2}{4}\left(\frac{U}{U_c}\right)^2 (1 - e_a \sin^2\vartheta)^{-2} I_1^{-2} - u' \frac{d}{4}\left(\frac{\gamma_2 \cos 2\vartheta - \gamma_1}{K_3}\right)\cos\varphi = 0\,. \tag{2}$$

(The factor $[1 - e_a \sin^2\vartheta]^{-2} I_1^{-2}$ represents the z-dependence of the electric field vector [6].)

From the balance of forces results an equation for the local velocity gradient $u'(\zeta)$:

$$\frac{\mathrm{d}}{\mathrm{d}\zeta}\left(\frac{\mathrm{d}u}{\mathrm{d}\zeta}\, g(\vartheta,\varphi)\right) = 0\,. \tag{3}$$

After integration with respect to the boundary conditions ($u(0) = v/2$, $u(1) = v$) we get

$$u' = \frac{v}{2}[I_2\, g(\vartheta,\varphi)]^{-1}\,, \tag{3a}$$

which is inserted into Equations (1), (2).

The following abbreviations are used:

$$' \triangleq \mathrm{d}/\mathrm{d}\zeta;\quad x_i = (K_i - K_3)/K_3;\quad f_i = 1 + x_i \sin^2\vartheta,\quad i = 1,2;\quad \gamma_K = (\gamma_2 - \gamma_1)/K_3 = 2\alpha_2/K_3;\quad U_c^2 = (-)\,\pi^2 K_3/\varepsilon_0\,\varepsilon_a,\quad \varepsilon_a = \varepsilon_\parallel - \varepsilon_\perp\ (<0); \tag{4}$$

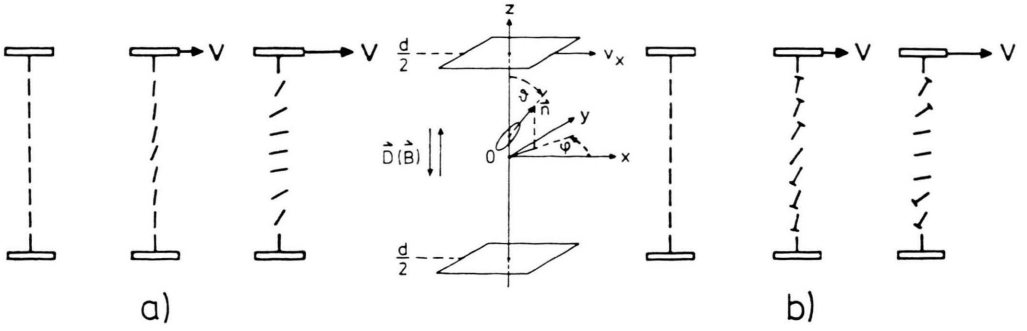

Fig. 2. Shear flow induced deformation profiles at different shear velocities v: a) nematic liquid crystal, b) cholesteric liquid crystal, the orientation of the director $\hat{n}$ is indicated by the currently used symbols | and ⊥, respectively.

$$I_1 = \int_0^1 (1 - e_a \sin^2 \vartheta)^{-1} \, d\zeta, \quad e_a = \varepsilon_a/\varepsilon_\parallel;$$

$$I_2 = \int_0^1 g(\vartheta, \varphi)^{-1} \, d\zeta,$$

$$g(\vartheta, \varphi) = \eta_1 \sin^2 \vartheta \cos^2 \varphi + \eta_2 \cos^2 \vartheta + \eta_3 \sin^2 \vartheta \sin^2 \varphi + \alpha_1 \sin^2 \vartheta \cos^2 \vartheta \cos^2 \varphi .$$

(η_i, $i = 1, 2, 3$ are the Miesowics [7] viscosity coefficients, α_i, $i = 1, \ldots, 6$ are the Leslie [2] viscosity coefficients, and $\gamma_1 = \alpha_3 - \alpha_2$, $\gamma_2 = \alpha_3 + \alpha_2$).

From a scale analysis [1, 8] of the differential equations follows that the solutions for ϑ and φ contain the experimental parameters only in certain combinations:

$$\vartheta = \vartheta(\zeta, v\,d, t_0\,d, U),$$
$$\varphi = \varphi(\zeta, v\,d, t_0\,d, U). \tag{5}$$

(The temperature T enters through the temperature dependence of the material constants of the liquid crystal.)

As already mentioned we will restrict the following calculations to the nematic case ($t_0 d = 0$, $\varphi(\zeta) = \varphi'(\zeta) = 0$). In this case Eqs. (1) and (2) reduce to one second order differential equation, which is hereafter referred to as Equation (2_n). This equation has to be solved for the boundary conditions $\vartheta(0) = \vartheta_m$, $\vartheta(-1) = \vartheta(+1) = 0$. The numerical computation method used is the following: First, the second order boundary value problem is reduced to an initial value problem with two coupled first order differential equations. Their integration is done by a fourth order predictor-corrector method of Hamming [9]. When starting the integration at $\zeta = 0$, the initial values are $\vartheta(0) = \vartheta_m$ and $\vartheta'(0) = 0$ (symmetry). Furthermore, a first choice of the integrals I_1 and I_2 is required. $\vartheta(0)$, which depends on the experimental parameters, is found by a shooting method: Starting with $\vartheta(0) = \pi/4$, the system of first order differential equations is repeatedly solved with a new properly chosen $\vartheta(0)$, until the second boundary value $\vartheta(1)$ lies close enough to zero (the integrals I_1 and I_2 are repeatedly computed by the well known Simpson method). For a shooting error of 0.2 to 0.5 per cent of ϑ_m the above outlined computation method converges typically after 8 to 12 iteration steps and takes about 4 seconds of computer time on the (relatively slow working) IMB 360/50 machine.

Using experimental values for the material constants of MBBA at room temperature listed in Table 1 (and data at other temperatures taken from the Refs. and Sect. 4) the solutions for $\vartheta(\zeta)$ are plotted in Fig. 3 for different parameters. In Fig. 3a the dependence of the tilt angle ϑ on the parameter vd is shown. The maximum tilt angle ϑ_m increases linearly with vd in the region of small vd and approaches the flow alignment angle $\vartheta_0 \approx 85°$ for $vd \to \infty$. At high values of vd, ϑ is nearly uniform in the whole layer with the exception of two boundary layers, in which ϑ steeply decreases to zero at the boundaries.

In Fig. 3b the experimental parameter is the reduced voltage U/U_c and vd is zero. Excluding the boundary layers, the director adapts a nearly parallel orientation to the boundaries at high U/U_c [6].

Figure 3c shows several plots of $\vartheta(\zeta)$ for a combination of shear flow and a (vertical) electric field. As expected, the electric field enlarges the shear induced tilt angle of the director even for $U/U_c < 1$. At sufficiently high values of U/U_c ϑ approaches the flow alignment angle ϑ_0 with increasing vd from values higher than ϑ_0, in contrast to the low field case.

ϑ is plotted in Fig. 3d as a function of the reduced temperature τ for a low and a high value of vd ($\tau = (T - T_c)/T_c$, where T_c is the absolute nematic-isotropic transition temperature). ϑ decreases with increasing temperature, whereas the thickness of the boundary layers increases.

The (reduced) local velocity $u(\zeta)d$ of the nematic liquid crystal is plotted in Fig. 4 for a) a low and b) a high value of vd respectively.

Table 1. Material constants at $\tau = -7 \times 10^{-2}$ used for numerical calculations of deformation profiles and effective optic anisotropoes (data with Ref. [a] are measured by the present author).

Constants		References
e_a =	$\varepsilon_a/\varepsilon_\parallel = -0.12$	[10], [a]
η_1 =	0.28	[11]
η_2 =	1.35	[11]
α_1 =	0.06 $\times 10^{-1}$ N s/m^2	[11]
γ_1 =	1.20	[a], from γ_K, γ_1/γ_2, K_3
γ_2 =	1.22	[a], from γ_K, γ_1/γ_2, K_3
U_c =	4.1 V	[a]
K_3 =	0.80×10^{-10} N	[a], from ε_a, U_c
$\varkappa_1$ =	-0.20	[a]
$n_\parallel$ =	1.789	[a]
$n_\perp$ =	1.555	[a]

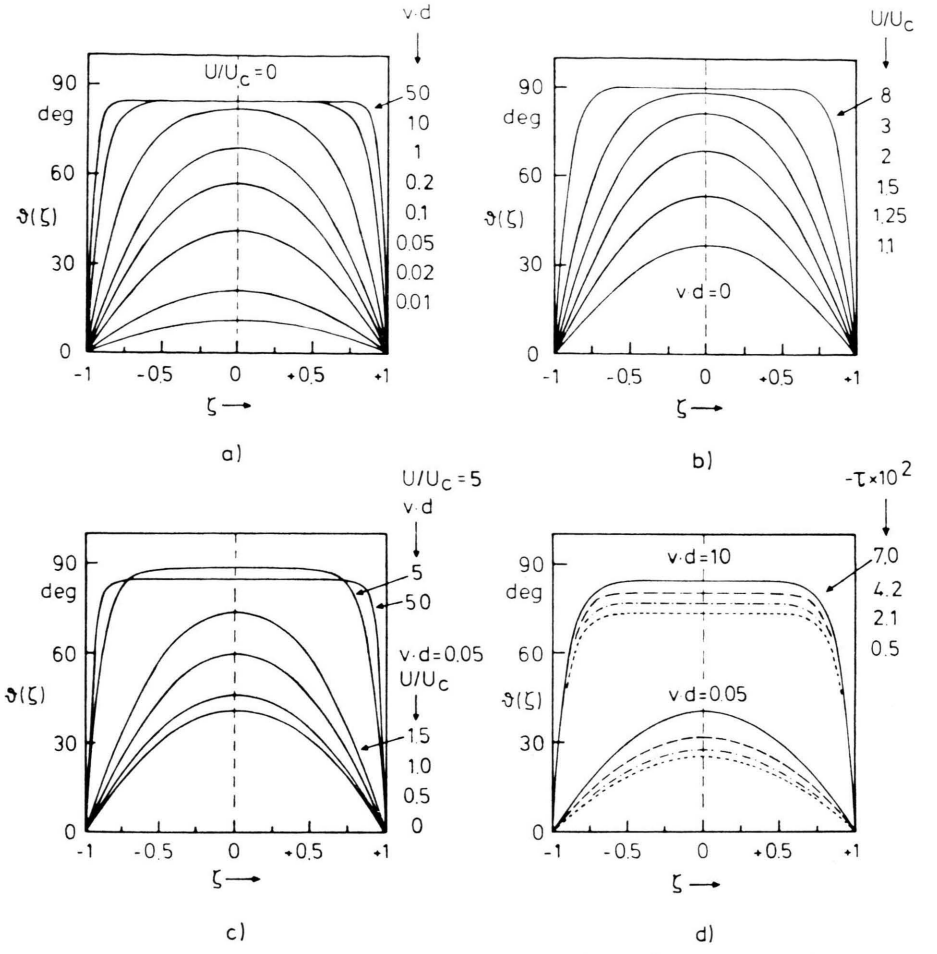

Fig. 3. Tilt angle $\vartheta(\zeta)$ of the director for different experimental parameters: a) vd (in units of 10^{-8} m²/s), b) U/U_c, c) vd and U/U_c, d) reduced temperature τ.

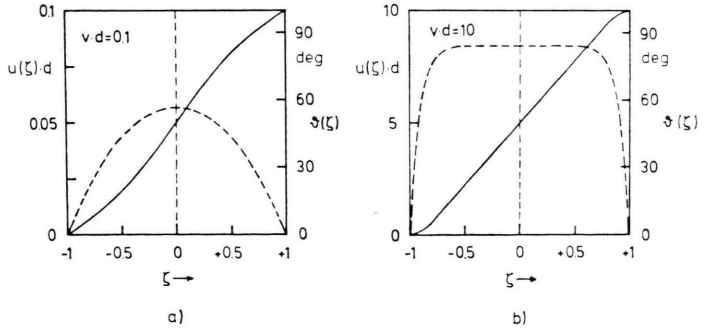

Fig. 4. $u(\zeta)d$ for a) a low and b) a high value of vd (dotted curve: $\vartheta(\zeta)$).

3.2. *Approximate Solution for Low vd and Low U/U_c*

For low tilt angles ϑ_m, Eq. (2_n) can be solved by the approximation

$$\vartheta(\zeta) = \vartheta_m[1 + (\varepsilon - 1)\zeta^2 - \varepsilon\zeta^4], \qquad (6)$$

as has been previously shown in detail for the most part [1, 12].

The parameters ϑ_m and ε can be deduced from the zeroth and first power in ϑ of a taylor expansion of Equation (2_n). Assuming a nearly constant

velocity gradient u' (see Fig. 4a) one obtains

$$\vartheta_m = -\frac{\gamma_K}{16R}\left[1+\frac{5}{3}\frac{P}{R}\right](v\,d) \tag{7}$$

$$\varepsilon = -\tfrac{1}{3}[W + P\,\vartheta_m^2], \tag{8}$$

with further abbreviations

$$W = \frac{\pi^2}{16}\left(\frac{U}{U_c}\right)^2; \quad p = x_1 S - \frac{16}{15} e_a W T;$$

$$R = 1 - \frac{5}{3} W; \quad S = 1 - \frac{2}{3} W;$$

$$T = 1 - \frac{2}{21} W. \tag{9}$$

It is assumed in the calculations that ϑ_m and ε are small quantities. Therefore the validity of the formulas (6)—(8) is restricted to low values for vd and U/U_c (for actual values see Section 4). In the small angle limit ($\vartheta_m < 0.5$) tilt angles $\vartheta(\zeta)$ obtained by Eq. (6) and those obtained by the computer calculations discussed in Sect. 3.1 agree very well. ϑ_m and ε diverge for negative dielectric anisotropy $\varepsilon_a = \varepsilon_\parallel - \varepsilon_\perp$ if W approaches the ratio 3/5 ($U/U_c = 0.98$). For $vd = 0$ and weak overcritical voltages $\vartheta(\zeta) = \vartheta_m \cos(\pi\zeta/2)$ is a good approximation of a solution of Eq. (2_n) [13].

Experimentally, the mean tilt angle $\overline{\vartheta}^\zeta$ of the director in the liquid crystal layer is indirectly given by measurements of the optic anisotropy of the layer:

$$\overline{n_e(\vartheta) - n_\perp}^\zeta = n_\perp \overline{\{[1 - N^2 \sin^2\vartheta]^{-1/2} - 1\}}^\zeta,$$

$$N = (1 - n_\perp^2/n_\parallel^2). \tag{10}$$

$n_e(\vartheta)$ is the refractive index of the extraordinary ray. $n_\parallel$ and $n_\perp$ are the refractive indices parallel and perpendicular to the director respectively. Observing the nematic layer between crossed polarizers (see Sect. 2), interference minima of order m occur if

$$m/d = \overline{(n_e(\vartheta) - n_\perp)}^\zeta/\lambda, \tag{11}$$

$$\approx \frac{n_\perp N}{2\lambda}\int_0^1 [\vartheta^2 + (\tfrac{3}{4}N - \tfrac{1}{3})\,\vartheta^4]\,\mathrm{d}\zeta \tag{12}$$

(for small ϑ).

Inserting Eqs. (6)—(8) into Eq. (12), the serial development of m/d reads

$$m/d = a_2(v\,d)^2 + a_4(v\,d)^4 + \cdots \tag{13}$$

with

$$a_2 = \frac{4}{15}\frac{n_\perp N}{\lambda}\gamma_K^2\, T/R^2 \tag{14}$$

$$a_4 = \frac{5}{2}\frac{a_2^2\lambda}{n_\perp N}\frac{1}{T^2}\left\{P[5/R^3 - 1/7] + \frac{2}{7}[3N - 4/3]Q\right\}; \quad Q = 1 - \frac{4}{33} W. \tag{15}$$

As discussed in Sect. 4, these equations allow to calculate some of the material constants of nematic liquid crystals, provided that the main refractive indices are known.

The approximation formalism outlined above can easily be applied to calculate time dependent changes of ϑ in the small angle limit:

$$\vartheta(\zeta, t) = \tilde{\vartheta}_m(t)\,\psi(\zeta) \tag{16}$$

with

$$\psi(\zeta) = [1 + (\sigma - 1)\,\zeta^2 - \sigma\,\zeta^4]$$

and

$$\tilde{\vartheta}_m(t) = \vartheta_m\, e^{st}.$$

The quantity s is a reciprocal time constant, which describes for $s < 0$ the relaxation of a distorted nematic layer into the homeotropic orientation. σ is a parameter, which is small compared to unity. The following analysis concerns to the reorientation of the director after stopping the shear flow at constant $U/U_c < 1$. The reorientation with a local angular velocity $\boldsymbol{\Omega}$ gives rise to translatory flow, called backflow [14]. Neglecting inertial terms [15], one obtains the following linearized equations from the balance conditions for force and torque respectively:

$$\frac{\mathrm{d}}{\mathrm{d}\zeta}\left(u'\,\eta_2 + \alpha_2\frac{d}{2}\dot{\vartheta}\right) = 0, \tag{17}$$

$$\vartheta'' - \frac{d}{2}\frac{\alpha_2}{K_3}u' + \frac{\pi^2}{4}\left(\frac{U}{U_c}\right)^2\vartheta - \frac{\gamma_1}{K_3}\frac{d^2}{4}\dot{\vartheta} = 0, \tag{18}$$

where $\dot{\vartheta}$ denotes the time derivative of ϑ.

With these equations one obtains:

$$\sigma = -\left[\frac{\pi^2}{48}\left(\frac{U}{U_c}\right)^2 + \frac{1}{4}\left(\frac{1-A}{A}\right)\right] \Big/ \left[1 + \frac{6}{5}\left(\frac{1-A}{A}\right)\right], \tag{19}$$

$$\frac{\gamma_1}{K_3}\,\mathrm{d}^2 s = [\pi^2(U/U_c)^2 + 48\sigma]/[1 - A]. \tag{20}$$

$A = \alpha_2^2/(\gamma_1\eta_2)$ is a viscosity parameter which results from the backflow terms in Eqs. (17) and (18).

The time constant s^{-1} should diverge for $U/U_c = 1$ ($vd = 0$). Because of using the approximation

formula (16) the location of the pole of s^{-1} is slightly differing from the point $U/U_c = 1$. (The relative deviation is typically lower than 1%.) Using the expression

$$\psi(\zeta) = \cos(\zeta\, k\, d/2) - \cos(k\, d/2)\,, \tag{21}$$

as done by Pieranski et al. [14], the requirement cited above is exactly fulfilled. But there is a disadvantage that the wave number k has to be calculated from a mixed goniometric equation. For low undercritical voltages however, the results of both approximations are in good agreement.

Experimentally, we measure the reciprocal decay time constant of the relaxation of the optic anisotropy of the layer. In a rough approximation we get from Equation (12):

$$m/d = \frac{n_\perp N}{2\lambda} \int_0^1 \vartheta^2(\zeta, t)\, \mathrm{d}\zeta\,.$$

By means of Eq. (16) one arrives at

$$m/d = (m/d)_i\, e^{2st}\,. \tag{22}$$

$(m/d)_i$ denotes the (m/d) of the stationary destorted layer.

3.3. Approximations for High vd or High U/U_c

In the case of high vd or high U/U_c the tilt angle ϑ is nearly constant in the whole layer excluding two boundary layers of a certain (relative) thickness ξ (see Sect. 3.1). According to a detailed derivation in a previous publication [1], ξ can easily be determined from Eq. (2_n) by approximating differentials by differences and averaging the other functions across a boundary layer

$$\xi = c_1\,[v\, d + c_2 (U/U_c)^2]^{-1/2}; \tag{23}$$

c_1 and c_2 contain material constants. For $vd = 0$, ξ formally agrees with the so-called electric coherence length [5].

For reasons of simplification we imagine a new, homeotropic boundary layer of relative thickness $\delta\xi$ $(0 < \delta < 1)$, or absolute thickness $d_b = \delta\xi d/2$. The actual anisotropy m/d of the whole layer is required to remain unchanged so that m/d is brought about by the effective thickness $d_{eff} = d - 2d_b$. If $(m/d)_0$ denotes the saturation value of m/d for $\xi = 0$, we have

$$\begin{aligned} m/d &= (m/d)_0\,\{1 - 2\delta\xi\} \qquad (24)\\ &= (m/d)_0\,\{1 - c_0[v\, d + c_2 (U/U_c)^2]^{-1/2}\} \\ &\qquad\qquad (c_0 = \text{const})\,, \end{aligned}$$

or

$$2d_b/d = 1 - (m/d)/(m/d)_0\,. \tag{25}$$

In the limiting case $vd < \infty$ and $U/U_c = \infty$ we obtain the saturation values $\vartheta_0 = 90°$ and $(m/d)_0 = (n_\parallel - n_\perp)/\lambda$. For $U/U_c < \infty$ and $vd = \infty$, ϑ_0 $(< 90°)$ represents the flow alignment angle, which is determined by the ratio γ_1/γ_2 of viscosity constants [2]:

$$\cos 2\vartheta_0 = \gamma_1/\gamma_2\,. \tag{26}$$

By means of Eq. (10) one obtains

$$\cos 2\vartheta_0 = 1 - 2(1 - M^{-2})/N\,, \tag{27}$$

with

$$M = (m/d)_0 (\lambda/n_\perp) + 1\,.$$

4. Discussion of Experimental Results

4.1. Refractive Indices and Interference Pattern

The measurements were carried out with nematic MBBA synthesized and purified by the author. The nematic-isotropic transition temperature T_c of fresh material was about 320 K. After filling the measuring cell with MBBA, T_c was about one degree lower due to absorption of impurities. In order to compare experimental data obtained with samples of different T_c, the reduced temperature scale with $\tau = (T - T_c)/T_c$ is used [16]. The nematic phase of MBBA ranges from $\tau = -0.082$ to $\tau = 0$, but often undercooling down to $\tau = -0.12$ was observed.

As indicated by the formulas in Sect. 3, the refractive indices $n_\parallel$ and $n_\perp$ (of MBBA) should be known precisely and therefore they have been separately measured for $\lambda = 546$ nm using an Abbe-refractometer (Figure 5). The maximum error of $n_\parallel$ and $n_\perp$ increases with increasing temperature from $\pm 1 \times 10^{-3}$ to $\pm 3 \times 10^{-3}$ and from $\pm 0.5 \times 10^{-3}$ to $\pm 2 \times 10^{-3}$ respectively. Excluding the high temperature range, the values in Fig. 5 agree within the error limits with values interpolated for $\lambda = 546$ nm from data published by Brunet-Germain [17]. Figure 5 also contains n_{is}, the refractive index of the isotropic phase, and the factor $N_\lambda = (n_\perp/\lambda)N$, which appears in Eqs. (14) and (15).

Figure 6 shows a typical interference pattern obtained by torsional shear flow of a nematic liquid crystal in the geometry of Figure 1. The system of concentric bright and dark interference rings is superposed by a black maltese cross, which indicates the vibration directions of the polarizers.

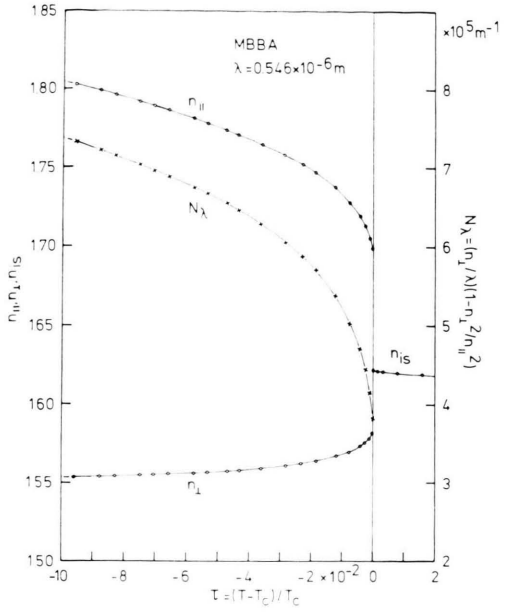

Fig. 5. Refractive indices of MBBA for wavelength $\lambda = 546$ nm.

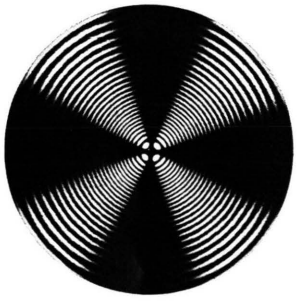

Fig. 6. Typical interference pattern (4/5 × nat. size) obtained by torsional shear flow of a nematic layer in a vertical electric field ($d = 150$ μm, $\omega = 2.5 \times 10^{-4}$/s, $U/U_c = 0.5$).

For a quantitative analysis of such interference patterns the experimental parameters like v, d, U/U_c, τ belonging to the different interference minima of order m are determined (see Refs. [1, 4] for more details).

4.2. Simple Shear Flow and Its Temperature Dependence ($U/U_c = 0$)

The ratio m/d is in general a function of the product vd, which has been shown by a scale analysis as well as by former experimental data [1]. Figure 7 shows plots of m/d as a function of vd for different values of the reduced temperature τ. All of the curves start at $vd = 0$ with a parabolic shape, which is indicated on the left part in an extended (vd)-scale. For $vd \to \infty$ the curves approach a temperature dependent saturation value $(m/d)_0$ as predicted by the theoretical analysis in Section 3. With increasing temperature m/d decreases, resulting from a decrease of $n_a = n_\parallel - n_\perp$ (see Fig. 5) and ϑ (see Figure 3d).

Let us now analyze the range of small vd according to the approximations in Section 3.2. The experimental points in Fig. 8 fit pretty well to a straight line for each τ. The intersection of these lines with the ordinate yields the parameter a_2. From the slope we get a_4 (see Eqs. (13), (14), (15)). Assuming the temperature dependence of the viscosity constants being mainly determined by an exponential factor [18], a_2 and a_4 should fit a straight line in an Arrhenius-plot. As can be seen from Fig. 9 such a behaviour holds only sufficiently below T_c. Today, there is only few knowledge about the temperature dependence of the material

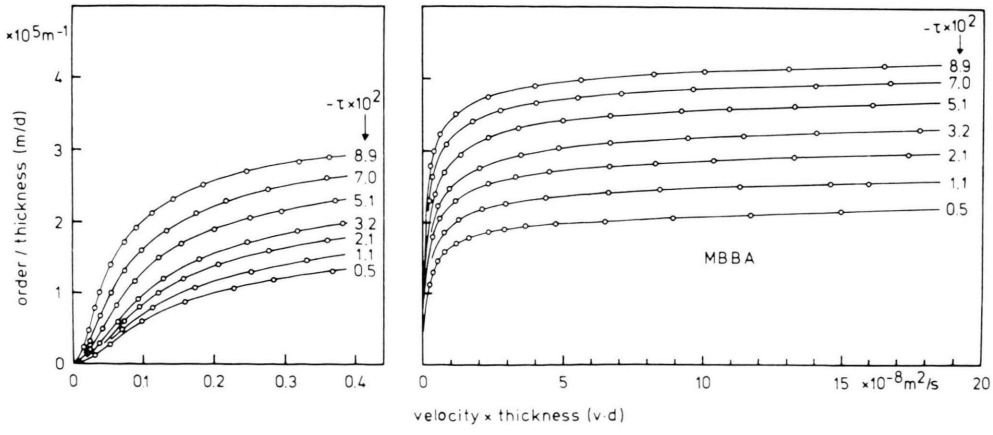

Fig. 7. m/d as a function of vd with τ as parameter.

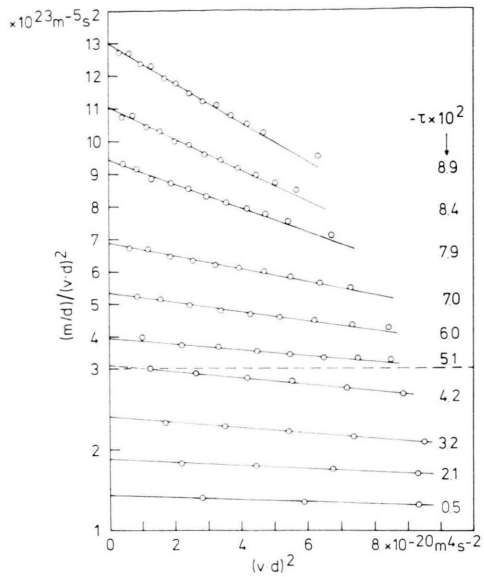

Fig. 8. Plot for determining the coefficients a_2 and a_4.

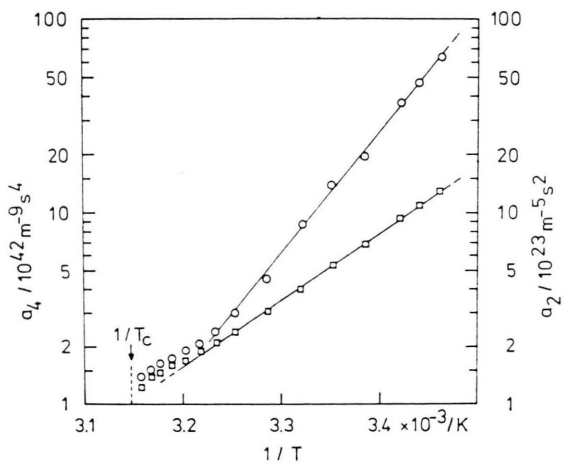

Fig. 9. Arrhenius plots of $a_2(\square)$ and $a_4(\circ)$.

constants of liquid crystals, so that we will omit to give an explanation for the deviation in the range near T_c. From a_2 (see Eq. (14)) the ratio $\gamma_K = (\gamma_2 - \gamma_1)/K_3$ of material constants can be calculated with a relative low error of 1,5% at low and 3% at high temperatures respectively. γ_K and a_2 are plotted in Fig. 10 as a function of τ. Up to now, no other measurements of γ_K are known from literature. Using data from literature for the single constants in γ_K [11, 19—21] one obtains a γ_K (with an error of about 20%) roughly agreeing with the present data.

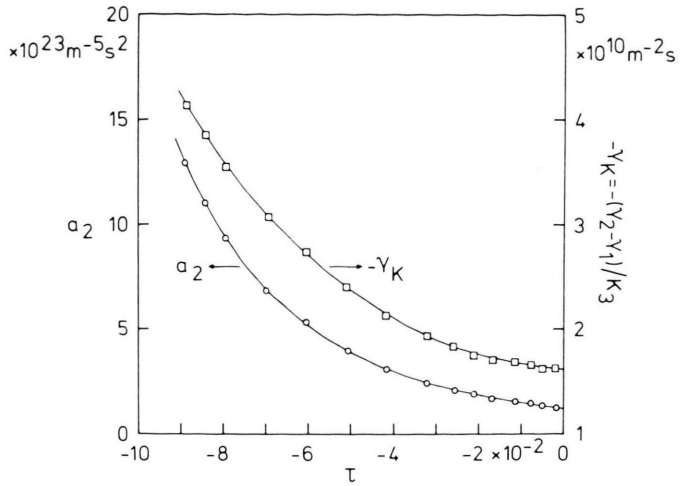

Fig. 10. Temperature dependence of a_2 and γ_K.

By means of Eq. (15) the ratio K_1/K_3 of the splay and bend elastic constants can be calculated from a_4. According to the Maier-Saupe theory [22] this ratio should be independent of temperature. The experimental points in Fig. 11 verify such a behaviour only within the limits of error.

We will now analyze the time dependent relaxation of a destorted nematic layer into the homeotropic orientation after stopping the shear flow. Figure 12 shows plots for the decay of m/d as a function of $(t - t_r)/d^2$ at different reduced temperatures. The curves are slided parallel to the abscissa in order to get the same (arbitrary) reference value $(m/d)_r$ at a time $t = t_r$. In such a representation the curves are independent of the layer thickness d as indicated for $\tau = -7 \times 10^{-2}$ and $\tau = -6 \times 10^{-2}$. Moreover, curves which start at different m/d, i.e. at different $v\,d$, coincide a short time after stopping

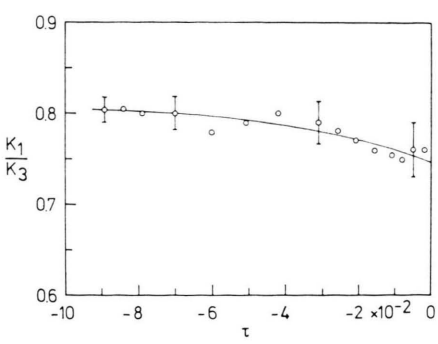

Fig. 11. Ratio K_1/K_3 of the splay and bend elastic constant of MBBA as calculated from a_2 and a_4.

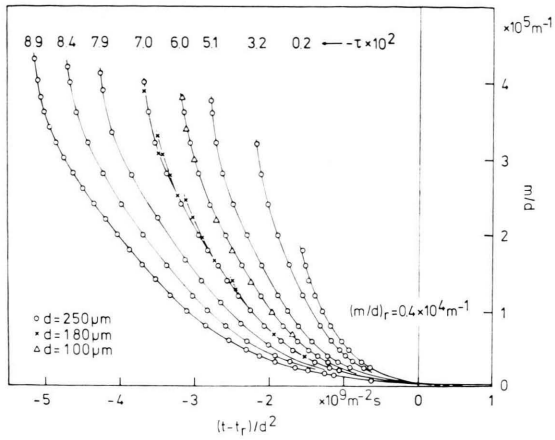

Fig. 12. Relaxation of m/d after stopping the torsional shear flow ($v\,d \to 0$).

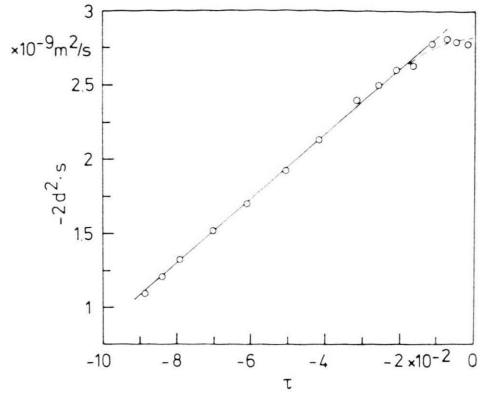

Fig. 14. Temperature dependence of the reciprocal decay time constant $2\,s$ (resp. $2\,s\,d^2$) of m/d.

the shear flow. This can be seen from the data for $\tau = -7 \times 10^{-2}$, obtained from single runs at four different $v\,d$. The steep decay of all curves immediately after stopping the shear flow is due to an inertial effect: The liquid crystal continues to flow a short time thus producing locally an additional reorienting torque (favouring homeotropic orientation), so that the decay of m/d is faster initially. The effective time of this flow relaxation is short compared to the time of reorientation into the homeotropic state. In the range of low tilt angles Fig. 13 verifies the exponential law (see Eq. (22)) for the relaxation of m/d. Excluding the high temperature range, the reciprocal time constant s decreases approximately linear with increasing temperature, as shown by Figure 14.

According to Eqs. (19) and (20) the reciprocal time constant s is not very sensitively determined by the constant $A = \alpha_2^2/(\gamma_1 \eta_2)$. This ratio of viscosity constants therefore has been calculated using the single constants $\gamma_K = (\gamma_2 - \gamma_1) K_3$, γ_1/γ_2 (see below), K_3 [20] and η_2 [11], in order to calculate the ratio γ_1/K_3 from the experimental data of s. γ_1/K_3 and A are plotted in Fig. 15 as a function of temperature. These values of γ_1/K_3 agree within an error limit of about 3% with values obtained from γ_K and γ_1/γ_2. From an Arrhenius plot of γ_1/K_3 one obtains for γ_1 an activation energy of 42 kJ/mole, which is about 10% lower than values given in literature [23, 24]. An advantage of this dynamical method of measuring γ_1/K_3 is that the refractive indices are not needed. If we would have neglected the backflow terms in the approximations of Sect. 3.3 (set $\alpha_2 = 0$), one would have obtained a reciprocal time constant s (using γ_1/K_3 from Fig. 15) which is about 20% higher than the experimental one (Figure 14). This very clearly confirms that the

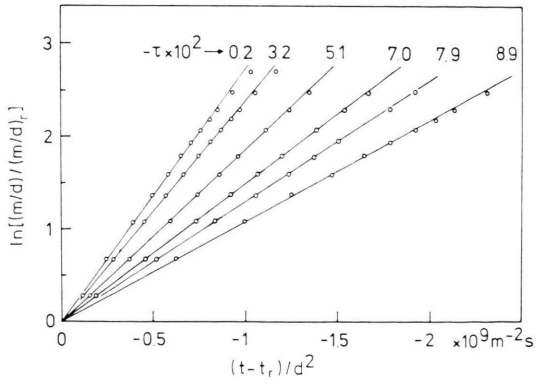

Fig. 13. Experimental veryfication of the exponential decay of m/d in the range of small deformation angles.

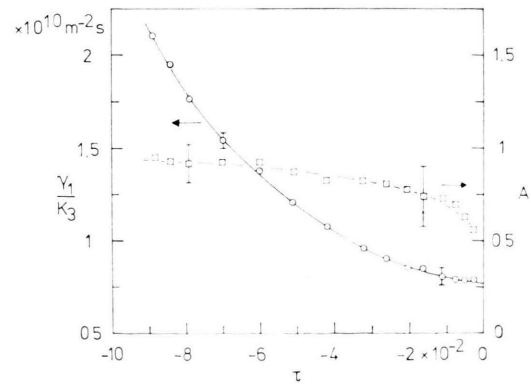

Fig. 15. Temperature dependence of γ_1/K_3 and $A = \alpha_2^2/(\gamma_1\,\eta_2)$.

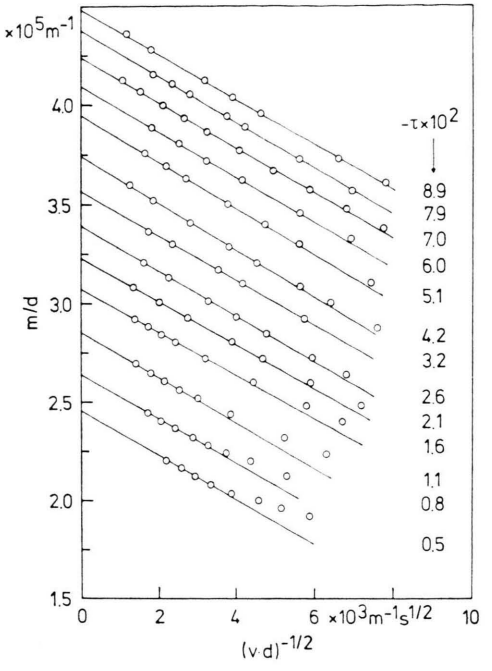

Fig. 16. m/d as a function of $(vd)^{-1/2}$ in the range of high vd (cp. Figure 7).

backflow terms should not be neglected in the homeotropic configuration [14].

By means of the approximations in Sect. 3.3 we will now analyze the curves of Fig. 7 in the range of high vd. Figure 16 veryfies Eq. (24) for different reduced temperatures τ. It is remarkable that the experimental points fit to straight lines of approximately the same slope

$$-c_0(m/d)_0 = -(11.5 \pm 0.5)\, s^{-1/2}.$$

The intersection of these lines with the ordinate yields the saturation value $(m/d)_0$, from which the flow alignment angle ϑ_0 and the ratio γ_1/γ_2 of viscosity constants can be calculated using Eqs. (26) and (27). The temperature dependence of these constants is shown in Figure 17. The error of ϑ_0 is strongly determined by the error of the refractive indices. Today, only few publications about measurements of ϑ_0 are known [25, 26]. In the limits of error the values of Gähwiller [25] are very close to the present ones (see Fig. 17), in contrast to those of Meiboom and Hewitt ([26], $\vartheta_0 \approx 72 \ldots 70$ deg). In Fig. 18 the relative thickness $2d_b/d$ of the

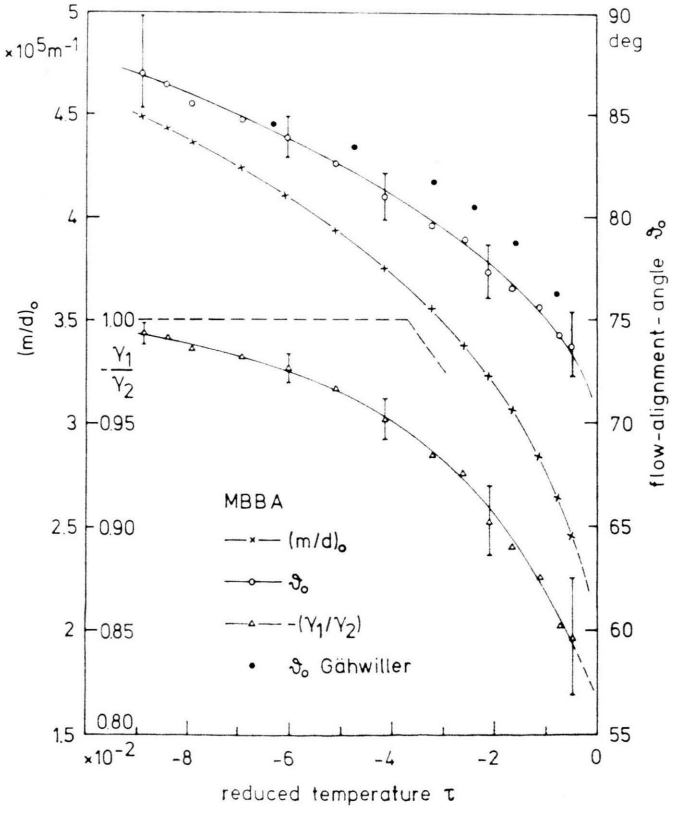

Fig. 17. Temperature dependence of $(m/d)_0$, ϑ_0, and γ_1/γ_2. The bars indicate the maximum errors as calculated from the uncertainties of the experimental quantities.

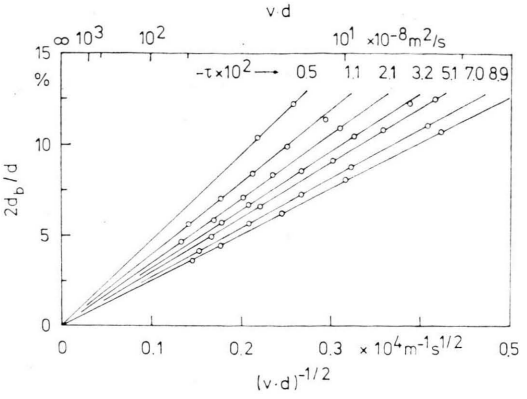

Fig. 18. Relative thickness $2d_b/d$ of the boundary layers at different reduced temperatures τ.

boundary layers is plotted against $(vd)^{-1/2}$ for different values of τ. The experimental points fit to straight lines through the origin with slopes c_0 ($\approx 11.5\, s^{-1/2}/(m/d)_0$). At constant vd the relative thickness of the boundary layers increases with temperature as predicted by the theoretical analysis in Section 3.1.

4.3. Simple Shear Flow in a Vertical Electric (Magnetic) Field

Figure 19 shows a plot analogeous to Fig. 7, now the reduced voltage U/U_c being the experimental parameter. Because of the negative dielectric anisotropy $\varepsilon_a = \varepsilon_\parallel - \varepsilon_\perp$ of MBBA, the electric field enlarges the flow induced value of m/d. With increasing overcritical voltage more and more interference rings are crowded around the center of torsion, in which the homeotropic orientation of the director still remains to exist* (for at least not too high U/U_c). This effect is indicated on the left part of Fig. 19 by the steep decrease of m/d (open points) in the range of very small vd. In order to obtain the correct shape of the (m/d)-curves (according to linear simple shear flow) in this range, they have been extrapolated for $vd \to 0$ to that m/d which is measured sufficiently far from the center of torsion some time (cp. Fig. 22) after stopping the shear flow. For $U/U_c \geqq 1$ the corrected (m/d)-curves then start at the origin with a non-zero slope.

Within an error range of about 0.5% to 5% the full data points in Fig. 19, calculated with a computer** as discussed in Sect. 3.1, agree very well with the experimental data (open points) all over the covered (vd)- and (U/U_c)-range. On the other hand, all of the material constants of the liquid crystal may in principle be determined by fitting computed data to experimental data in those (vd)- and (U/U_c)-ranges, in which m/d is most sensitive to the single constants. In practice however, the error limits of many of the material constants will come out too high.

* The corresponding deformation structure in the central region of the cell is that of an umbilic [5] studied in detail in a forthcoming paper.

** In these calculations the material constants of Table 1 are used.

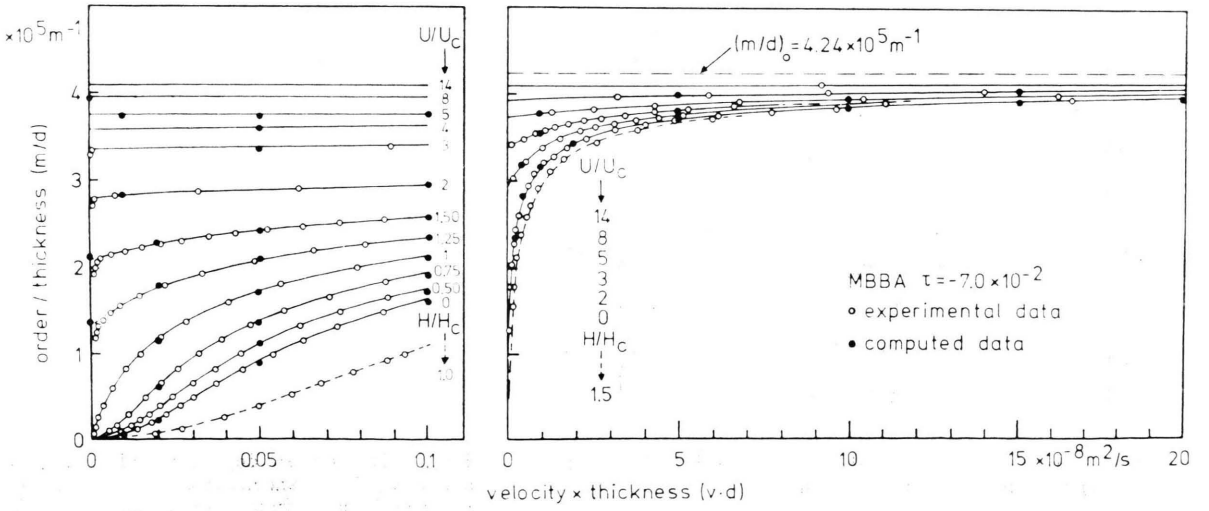

Fig. 19. m/d as a function of vd with U/U_c (H/H_c) as parameter.

The range of low vd may be analyzed for $U/U_c<1$ in the same way as before in Section 4.2. Figure 20 veryfies the theoretically predicted increase of the coefficients a_2 and a_4, from which a new ratio of material constants can additionally be determined:

$$-\varepsilon_a/K_3 = (7.0 \pm 0.04) \times 10^{10}\, N^{-1} \qquad (28)$$
$$(\tau = -7 \times 10^{-2})\,.$$

Figure 21 indicates a relatively good agreement between theoretical and experimental values of a_2 and a_4 for $U/U_c<0.5$.

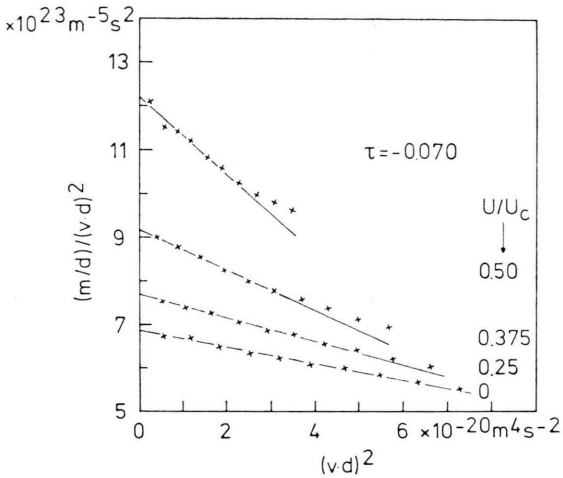

Fig. 20. Plot for determining the coefficients a_2 and a_4 for different undercritical values of U/U_c.

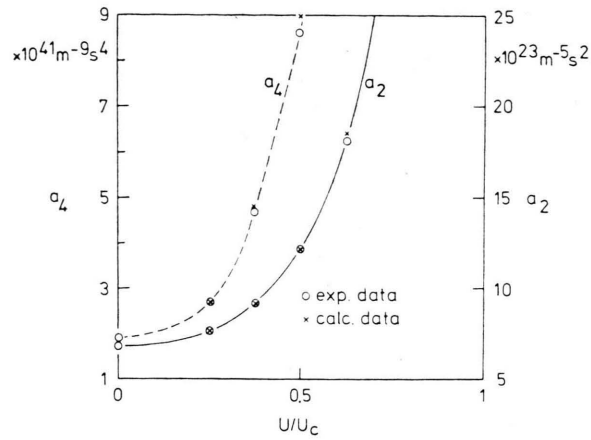

Fig. 21. Theoretical and experimental values of a_2 and a_4 as a function of U/U_c ($\tau = -7 \times 10^{-2}$).

In reduced coordinates Fig. 22 shows the time dependent decay of m/d to an equilibrium value $(m/d)_e$ after stopping the shear flow at constant U/U_c (cp. Figure 12). The curves are slided parallel to the abscissa, so that (at $t = t_r$) $(m/d)_r$ is (arbitrarily) $1 \times 10^4\ m^{-1}$ higher than $(m/d)_e$ for all curves. From the experimental data in Fig. 22 one obtains reciprocal time constants s agreeing for $U/U_c<0.5$ very well with theoretical ones obtained by means of γ_1/K_3 and A from Figure 15. This is shown by Fig. 23, which also gives the calculated voltage dependence of the parameter σ (see Equation (19)).

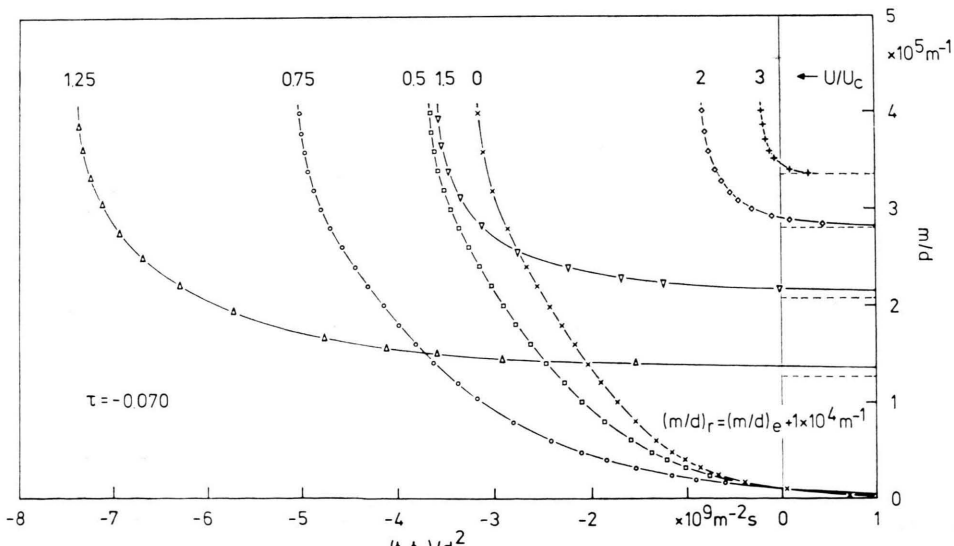

Fig. 22. Relaxation of m/d after stopping the torsional shear flow at different (constant) U/U_c.

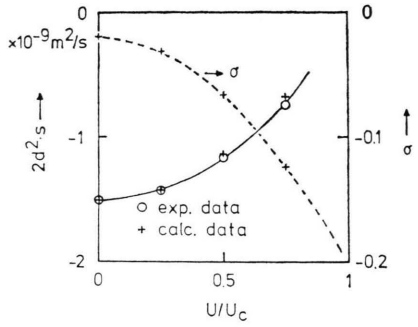

Fig. 23. Reciprocal time constant $2s$ (resp. $2sd^2$) and parameter σ as a function of U/U_c ($\tau = -7 \times 10^{-2}$).

Plotting $-2d^2s$ against $(U/U_c)^2$ one gets a straight approximation line from which the material constants γ_1/K_3 and A can be calculated separately. For $\tau = -0.070$ their values agree within an error limit of 5% with those in Figure 15.

Analyzing the curves in Fig. 19 in the range of high vd by plotting m/d against $(vd)^{-1/2}$ one finds that the experimental points deviate with increasing U/U_c more and more from the approximation line for $U/U_c = 0$ (cp. Fig. 16, $\tau = -0.070$). Such a behaviour is expected according to Equation (24).

As indicated by the (lower) dashed curve in Fig. 19, a (reduced) vertical magnetic field H/H_c lowers the effective optic anisotropy m/d because of the positive diamagnetic anisotropy $\chi_a = \chi_\parallel - \chi_\perp$ of MBBA. Therefore, applying both an electric and a magnetic field, the counteracting electromagnetic torques can be compensated with a proper ratio of fields. In this case the radius of an interference minimum of order $m \geqq 1$ will remain unchanged (at constant vd). Neglecting the depolarization effect (see comment to Eq. (2)), the balance condition of electromagnetic torques yields:

$$-\varepsilon_0 \varepsilon_a U^2 = \mu_0 \chi_a (H d)^2 . \tag{29}$$

This equation is veryfied by Figure 24. From the slope of the approximation line we obtain the ratio ε_a/χ_a of material constants

$$-\varepsilon_a/\chi_a = (3.8 \pm 0.1) \times 10^5 , \tag{30}$$

which agrees within the limits of error with values calculated from data for the single constants given in literature [27, 28].

Similarly, we may compensate the counteracting fields at the critical transition from the homeotropic to the distorted orientation (Frederiks transition [5]) of the liquid crystal. The critical voltage U_c is raised to $U_{c'}$ if a vertical magnetic field $H_{c'}$ is

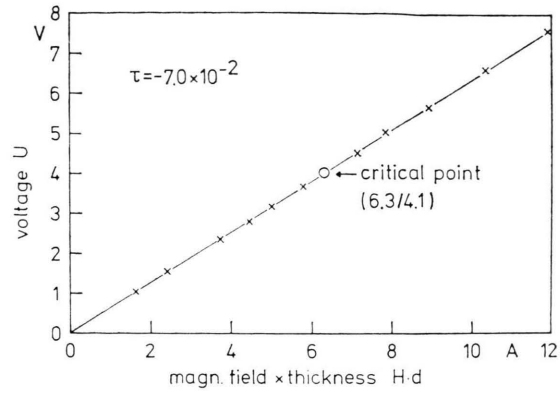

Fig. 24. Compensation of electric and magnetic fields for interference orders $m \geqq 1$.

simultaneously applied:

$$U_{c'}^2 = U_c^2 - \frac{\mu_0 \chi_a}{\varepsilon_0 \varepsilon_a} (H d)_{c'}^2 . \tag{31}$$

Such a behaviour is confirmed by the experimental points in Figure 25. From the slope of the straight line we get

$$-\varepsilon_a/\chi_a = (3.5 \pm 0.4) \times 10^5 . \tag{32}$$

The compensation method is most sensitive in the range of medium interference orders m. Experimentally, the compensation is favourably carried out with a nonuniformly distorted liquid crystal layer like that obtained by torsional shear (see Figure 6). Knowing ε_a from other measurements*,

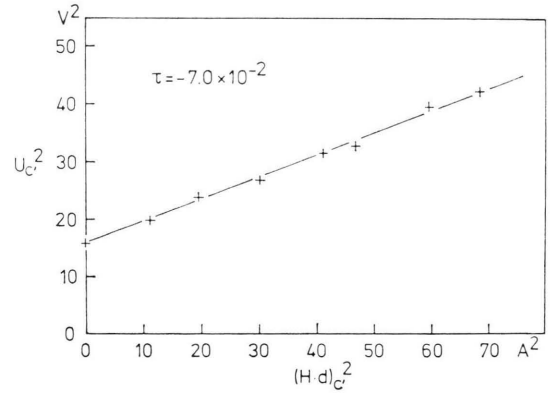

Fig. 25. Increase of the critical voltage U_c of the (electric) Frederiks transition.

* With the apparatus described in Sect. 2, $\varepsilon_a = \varepsilon_\parallel - \varepsilon_\perp$ can be determined from capacitance measurements as follows: $\varepsilon_\parallel$ is easily measured in the homeotropic configuration. $\varepsilon_\perp$ is deduced from the capacitance of a strongly distorted homeotropic layer (high angular velocities), using $\varepsilon_\parallel$ and the experimental values for ϑ_0 and d_b/d (see Secs. 3.3 and 4.2).

the compensation of electric and magnetic fields may be regarded as a simple and rather precise method of determining χ_a (and vice versa). Moreover, each of the single material constants occurring in the ratios determined in Sect. 4 may be calculated if one of these constants is known (e.g. ε_a).

5. Conclusion

In a recently published paper [29] it has been pointed out that the torsional shear flow method may advantageously be applied in large fields of liquid crystal research. Besides studying simple shear flow this method is very powerful for investigating shear induced texture transitions as well as inversion and domain structures (Part II and forthcoming papers). The present paper is restricted to a broad summary of partially new studies of simple shear flow of nematic liquid crystals in an electric field of frequency $f \approx 1$ kHz. (In the dc- or low frequency ac-regime, the simple shear flow is superposed by cellular electrohydrodynamic motions of the liquid crystal, thus obtaining shear induced transitions between uniform textures and domain textures, [30]). The experimental data are shown to agree very well with the theoretically predicted ones. Concerning the determination of material constants only, it should be emphasized at this point, that some of the viscosity and elastic constants may be measured more easily (though in general not more exactly) with partially less experimental equipment using well known techniques described in literature [20, 31, 11, 19, 32, 33, 34]. On the other hand, the torsional shear flow method is more universal in liquid crystal research as cited above.

Acknowledgement

Part of this work was supported by the Deutsche Forschungsgemeinschaft.

[1] J. Wahl and F. Fischer, Mol. Cryst. Liq. Cryst. **22**, 359 (1973).
[2] F. M. Leslie, Arch. Rat. Mech. Anal. **28**, 265 (1968).
[3] J. L. Ericksen, Mol. Cryst. Liq. Cryst. **7**, 153 (1969).
[4] F. Fischer, J. Wahl, and Th. Waltermann, Ber. Bunsenges. physik. Chem. **78**, 891 (1974).
[5] P. G. de Gennes, The Physics of Liquid Crystals, Clarendon Press, Oxford 1974.
[6] H. J. Deuling, Mol. Cryst. Liq. Cryst. **19**, 123 (1972).
[7] M. Miesowics, Nature **158**, 27 (1946).
[8] J. L. Ericksen, Trans. Soc. Rheol. **13**, 9 (1969).
[9] IBM Scientific Subroutine Package, p. 337.
[10] D. Diguet, F. Rondelez, and G. Durand, C. R. Acad. Sci. Paris **271 B**, 954 (1970).
[11] Ch. Gähwiller, Mol. Cryst. Liq. Cryst. **20**, 301 (1973); Phys. Lett. **36 A**, 311 (1971).
[12] Th. Waltermann and F. Fischer, Z. Naturforsch. **30 a**, 519 (1975).
[13] G. Labrunie and H. Robert, J. Appl. Phys. **44**, 4869 (1973).
[14] P. Pieranski, F. Brochard, and E. Guyon, J. Physique **34**, 35 (1973).
[15] G. Heppke and F. Schneider, Z. Naturforsch. **29 a**, 1356 (1974).
[16] I. Haller, H. A. Higgins, and M. J. Freiser, Mol. Cryst. Liq. Cryst. **16**, 53 (1972).
[17] M. Brunet Germain, C. R. Acad. Sci. Paris **271 B**, 1075 (1970).
[18] F. Jähnig, Proc. Bangalore Liq. Cryst. Conf., Pramana, Suppl. **1**, 31 (1975).
[19] J. Prost and H. Gasparoux, Phys. Lett. **36 A**, 245 (1971).
[20] I. Haller, J. Chem. Phys. **27**, 1400 (1972).
[21] J. Robert, G. Labrunie, and J. Borel, Mol. Cryst. Liq. Cryst. **23**, 197 (1973).
[22] A. Saupe, Z. Naturforsch. **15 a**, 810 (1960).
[23] P. J. Flanders, Mol. Cryst. Liq. Cryst. **29**, 19 (1974).
[24] G. Heppke and F. Schneider, Z. Naturforsch. **27 a**, 976 (1972).
[25] Ch. Gähwiller, Phys. Rev. Lett. **28**, 1554 (1972).
[26] S. Meiboom and R. C. Hewitt, Phys. Rev. Lett. **30**, 261 (1973).
[27] H. Gasparoux and J. Prost, J. Physique **32**, 953 (1971).
[28] P. I. Rose, Mol. Cryst. Liq. Cryst. **26**, 75 (1974).
[29] J. Wahl, 7th Int. Liq. Cryst. Conf. Bordeaux 1978, J. Physique Coll. **40**, C 3—98 (1979).
[30] J. Wahl, to be published.
[31] M. Greulich, G. Heppke, and F. Schneider, Z. Naturforsch. **30 a**, 515 (1975).
[32] Orsay Liq. Cryst. Group, J. Chem. Phys. **51**, 816 (1969).
[33] P. Martinoty and S. Candau, Mol. Cryst. Liq. Cryst. **14**, 243 (1971).
[34] J. C. Bacri, J. Physique Lett. **35**, L 141 (1974).